JOURNAL OF SYNCHROTRON RADIATION

ISSN 1600-5775

Vibrational stability improvement of a mirror system using active mass damping

Shijing He, Haoran Yuan, Tianyu Wu, Nuo Chen, Xinyu Zhang, Zhizhuo Wang, Xuerong Liu and Fang Liu*

Center for Transformative Science, ShanghaiTech University, 393 Huaxia Middle Road, Shanghai 201210, People's Republic of China. *Correspondence e-mail: liufang@shanghaitech.edu.cn

Received 17 April 2024
Accepted 2 July 2024

Edited by R. W. Strange, University of Essex, United Kingdom

Keywords: active vibration control; active mass damper; spillover effect; free-electron laser.

Addressing the demand for high stability of beamline instruments at the SHINE facility, a high stability mirror regulating mechanism has been developed for mirror adjustments. Active mass damping was adopted to attenuate pitch angle vibrations of mirrors caused by structural vibrations. An internal absolute velocity feedback was used to reduce the negative impact of spillover effects and to improve performance. The experiment was conducted on a prototype structure of a mirror regulating mechanism, and results showed that the vibration RMS of the pitch angle was effectively attenuated from 47 nrad to 27 nrad above 1 Hz.

1. Introduction

Advanced X-ray light sources have become very important tools for research in modern science applications due to their high brightness, short pulse and good coherence. Compared with traditional synchrotron radiation sources, free-electron lasers (FELs) are characterized by higher peak brightness, shorter pulse width and better coherence (Pellegrini & Stöhr, 2003; Zhao & Feng, 2018), and are hence considered to be a new generation of light sources (Georgescu, 2020). As part of the Zhangjiang scientific facility group of advanced light sources, Shanghai High repetitioN rate XFEL and Extreme light facility (SHINE) is expected to achieve ultra-high peak brightness and average brightness, high repetition rate and femtosecond-level ultrafast pulses, as well as nanoscale ultra-high spatial resolution and femtosecond level ultrafast time resolution.

X-ray beam transportation is up to 1 km long, in order to take full advantage of the surface smoothness of the beamline optical devices (Siewert *et al.*, 2019), as well as the pointing stability – the angular demands of mirrors in the transportation should be less than 50 nrad. For such high requirements, disturbance from the tunnel floor, motion devices and cooling devices (Li *et al.*, 2011) cannot be ignored. Most of the disturbances will be attributed to structural vibrations of mechanical structures which will then affect the beam transportation stability (Houghton *et al.*, 2021).

In order to improve the stability of instruments at advanced light sources, passive vibration isolation (Mangra *et al.*, 1996; Van Vaerenbergh *et al.*, 2008) is generally used in engineering: the influence of vibration on the instrument is improved by optimizing the physical design of the mechanical structure. However, passive vibration isolation is a poor suppression effect for low-frequency vibrations. Furthermore, it is difficult

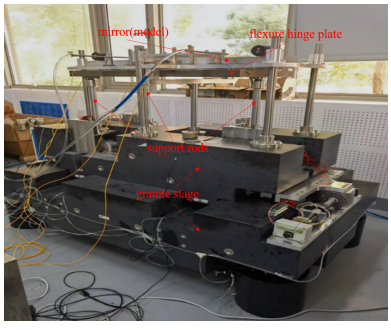

to increase damping in a vacuum, and damping materials age quickly (Liu *et al.*, 2020).

With the development of microelectronics technology, research is increasingly focused on the active vibration reduction method, which can effectively damp structural resonances and low-frequency vibrations (Guoping *et al.*, 2004), with good flexibility. For active vibration control, the actuator arrangement of active vibration isolation is often limited by the actual mechanical structure, while the actuator position of active mass damping (AMD) (Gonzalez Diaz, 2007) is independent. However, AMD could cause serious resonance at its natural frequency (required to be lower than the controlled band), called the 'spillover effect', so the problem caused by the 'spillover effect' is intolerable for all-frequency sensitive applications.

In this work, an internal absolute velocity feedback (IAVF) is proposed for AMD to reduce the influence of the spillover effect, and to improve the modal vibration damping performance of the controlled structure. The angular pitch vibration attenuation performance was demonstrated on a mirror-adjusting mechanism for the SHINE project.

2. Model of active mass damping

To attenuate structural vibrations, AMD is introduced. For simplicity, a two-degrees-of-freedom model is built. The principle of AMD is shown in Fig. 1, where m_1 is the mass of the controlled structure and m_2 is the mass of the active mass damper (AMDer). The dynamic equation of the system is

$$m_2 s^2 X_2 = -(c_2 s + k_2)(X_2 - X_1) + F, \tag{1}$$

$$m_1 s^2 X_1 = -(c_1 s + k_1)(X_1 - X_0) - (c_2 s + k_2)(X_1 - X_2) - F, \tag{2}$$

where $X_1(s)$, c_1 and k_1 are the Laplace transform of the absolute displacement, damping coefficient and stiffness of the controlled structure, respectively; $X_2(s)$, c_2 and k_2 are the Laplace transform of the displacement, damping coefficient and stiffness of the AMDer, respectively. F is the secondary force generated by a voice coil motor (VCM), expressed as

$$F = \frac{K_\mathrm{f}}{(1 + s\tau)\,R}\,U, \tag{3}$$

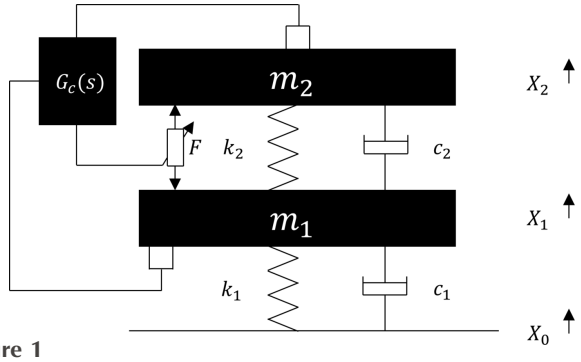

Figure 1
Two-degrees-of-freedom model of the active mass damping system.

where K_f, R and τ are the force constant, coil resistance and electrical time constant of the VCM, respectively (the back electromotive force was ignored here). U is the driving voltage of the VCM computed by the feedback controller, which, in the ordinary AMD, is described as

$$U = G_{c1}(-X_1), \tag{4}$$

and the PID control algorithm G_{c1} is simply expressed as

$$G_{c1} = D_1 s^2 + P_1 s + I_1. \tag{5}$$

To reduce the spillover effect and improve the modal vibration attenuation performance, an IAVF is introduced to increase the active damping of the AMDer. A control diagram is illustrated in Fig. 2, according to which the driving voltage of the VCM became

$$U = G_{c1}(-X_1) + G_{c2}(-X_2), \tag{6}$$

where

$$G_{c2} = P_2 s \tag{7}$$

is part of the control algorithm for IAVF. According to all formulas above, with

$$p_{v1} = \frac{K_\mathrm{f}}{R} P_1, \qquad p_{x1} = \frac{K_\mathrm{f}}{R} I_1, \qquad p_{a1} = \frac{K_\mathrm{f}}{R} D_1, \tag{8}$$

$$U' = G_{c1}(-X_1) \tag{9}$$

and

$$p_{v2} = \frac{K_\mathrm{f}}{R} P_2, \tag{10}$$

the vibrational transfer function from ground to controlled object, G_{p1}, and that from U' to controlled object vibration, G_{s1}, are expressed as

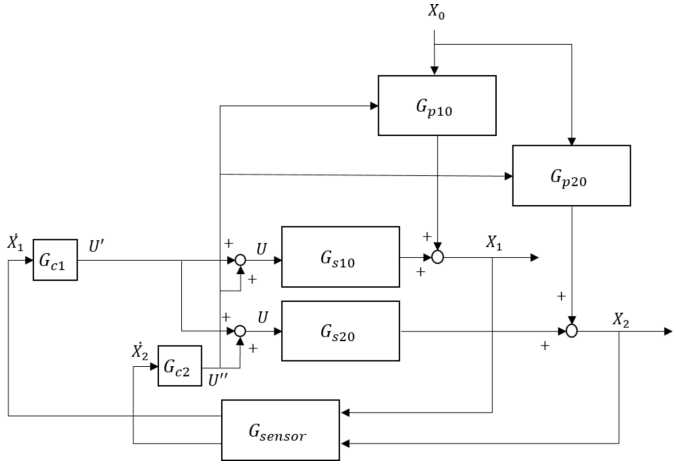

Figure 2
Control diagram of AMD with IAVF.

$$G_{p1}=\frac{X_1}{X_0}\bigg|_{U'=0}=\Big\{\big[(m_2s^2+c_2s+k_2)(1+s\tau)+p_{v2}s\big](c_1s+k_1)\Big\}\Big/\Big\{m_2s^2\big[(m_1s^2+c_1s+k_1)+(c_2s+k_2)\big](1+s\tau)+(m_1s^2+c_1s+k_1)\big[(c_2s+k_2)(1+s\tau)+p_{v2}s\big]\Big\},\quad(11)$$

$$G_{s1}=\frac{X_1}{U'}\bigg|_{X_0=0}=-(K_f/R)\Big((m_2s^2)\Big/\Big\{m_2s^2\big[(m_1s^2+c_1s+k_1)+(c_2s+k_2)\big](1+s\tau)+(m_1s^2+c_1s+k_1)\big[(c_2s+k_2)(1+s\tau)+p_{v2}s\big]\Big\}\Big),\quad(12)$$

and the vibrational transfer function from the ground to the internal mass of the AMDer, G_{p1}, and that from U' to the internal mass of the AMDer, G_{s1}, are expressed as

$$G_{p2}=\frac{X_2}{X_0}\bigg|_{U'=0}=\big[(c_1s+k_1)(c_2s+k_2)(1+s\tau)\big]\Big/\Big\{m_2s^2\big[(m_1s^2+c_1s+k_1)+(c_2s+k_2)\big](1+s\tau)+(m_1s^2+c_1s+k_1)\big[(c_2s+k_2)(1+s\tau)+p_{v2}s\big]\Big\},\quad(13)$$

$$G_{s2}=\frac{X_2}{U'}\bigg|_{X_0=0}=\frac{K_f}{R}\Big((m_1s^2+c_1s+k_1)\Big/\Big\{m_2s^2\big[(m_1s^2+c_1s+k_1)+(c_2s+k_2)\big](1+s\tau)+(m_1s^2+c_1s+k_1)\big[(c_2s+k_2)(1+s\tau)+p_{v2}s\big]\Big\}\Big).\quad(14)$$

In particular, the definitions of G_{p10}, G_{s10}, G_{p20}, G_{s20} in Fig. 2 are, respectively,

Table 1
Parameters of the AMD model.

Mass of controlled structure, m_1	10^{-5}
Damping rate of controlled structure, ξ_1	0.05
Natural frequency of controlled structure, ω_1	$2\pi \times 25$ Hz
Internal mass of AMDer, m_2	10^{-6}
Damping rate of AMDer, ξ_2	0.04
Natural frequency of AMDer, ω_2	$2\pi \times 5.5$ Hz
Electrical time constant, τ	1.5 ms

$$G_{p10}=G_{p1}\big|_{p_{v2}=0},\qquad G_{s10}=G_{s1}\big|_{p_{v2}=0},\qquad G_{p20}=G_{p2}\big|_{p_{v2}=0},\qquad G_{s20}=G_{s2}\big|_{p_{v2}=0}.\quad(15)$$

Considering the closed-loop transfer function by Fig. 2 (ignoring the dynamic characteristic of sensor),

$$\frac{X_1}{X_0}=\frac{G_{p1}}{1-sG_{s1}G_{c1}},\quad(16)$$

the control performance

$$\frac{X_1}{X_0}=\Big\{\big[(m_2s^2+c_2s+k_2)(1+s\tau)+p_{v2}s\big](c_1s+k_1)\Big\}\Big/\Big\{m_2s^2\big[(m_1s^2+c_1s+k_1)+(c_2s+k_2)\big](1+s\tau)+m_2s^2(p_{a1}s^2+p_{v1}s+p_{x1})+(m_1s^2+c_1s+k_1)\big[(c_2s+k_2)(1+s\tau)+p_{v2}s\big]\Big\},\quad(17)$$

reflects the transmissibility from the ground to the controlled structure with AMD. In this work, velocity feedback was mainly adopted, since it is effective for multi-mode attenuation.

According to formula (12), the open-loop frequency response (OLFR) of the unit-gain velocity feedback,

$$G_{\rm OLFR}=-sG_{s1},$$

with the parameters listed in Table 1 is shown in Fig. 3(*a*). There are two resonant peaks in the amplitude–frequency response curve: one with lower natural frequency and lower amplitude, which is caused by the AMDer, the other with higher natural frequency and higher amplitude, which is from

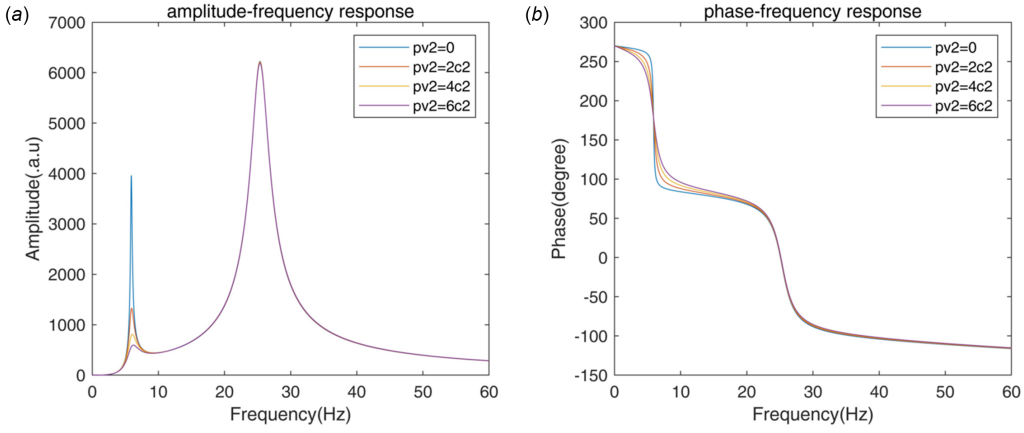

Figure 3
Open-loop frequency response of unity gain exterior velocity feedback.

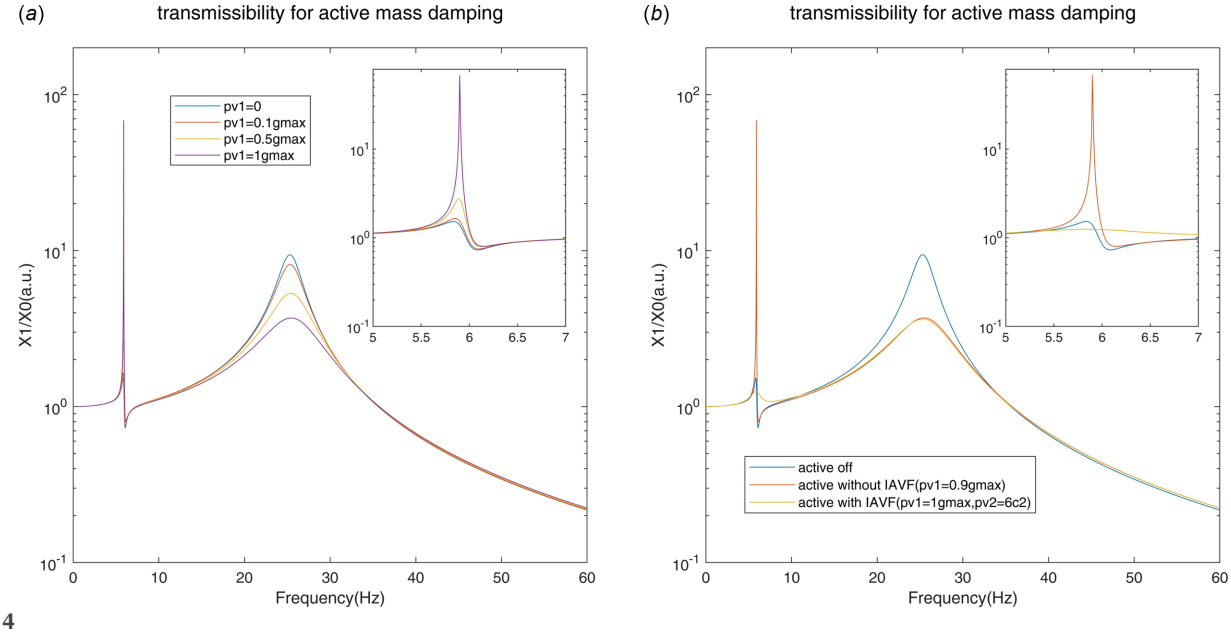

Figure 4
Transmissibility for AMD without IAVF (*a*) and with IAVF (*b*).

the mode of the controlled structure. For the phase–frequency response curve, the phase starts from 270° at 0 Hz, shows lag from about 250° to about 90° around the natural frequency of resonance of the AMDer, from about 70° to about −100° is around the natural frequency of the resonance of the controlled structure, and continues the lag slowly as the frequency increases. The crossing at 180° of the phase near the natural frequency of the resonance of the AMDer implies the spillover effect: the vibration of the closed-loop system at this frequency will be amplified when the gain increases, and divergent when the gain exceeds the margin. The influence of IAVF gain, p_{v2}, is considered: as p_{v2} increases, the peak values of the open-loop amplitude–frequency response at the natural frequency of the AMD, $|G_{\rm OLFR}(j\omega_a)|$, drops visibly, while the amplitude at the kth natural frequency of the controlled structure, $|G_{\rm OLFR}(j\omega_k)|$, is almost invariant. According to

$$R(\omega_k) = 20\log\left(1 + \frac{|G_{\rm OLFR}(j\omega_k)|}{|G_{\rm OLFR}(j\omega_a)|}\right) = 20\log(1+\delta_{k0}), \quad (18)$$

the stability–performance formula proposed by Gonzalez Diaz (2007), where $\delta_{k0} = |G_{\rm OLFR}(j\omega_k)|/|G_{\rm OLFR}(j\omega_a)|$, the performance of modal vibration attenuation could be improved by IAVF.

According to formula (17), the transmissibility of AMD is shown in Fig. 4. The active damping effect at the natural frequency of the controlled structure is significantly improved as the gain [$g_{\rm max} = 1/|G_{\rm OLFR}(j\omega_a)|$] is raised; however, the spillover effect at the natural frequency of the AMDer increases. With the IAVF, it is obvious that the increase at AMD resonance is suppressed, while the same vibration attenuation performance is achieved at the resonance of the controlled structure. As a cost, the frequency range of the spillover effect is widened due to the active damping effect of IAVF.

3. Introduction of a test setup

To test the performance of the AMDer with IAVF, a prototype of the AMDer was built, installed and tested at the mirror regulating mechanism for the SHINE offset mirror.

3.1. Introduction of the mirror regulating system

The whole adjusting mechanism was designed as shown in Fig. 5. A detailed description has been given by Liu *et al.* (2023). A double-layer granite base was used for coarse pitch angle adjustment and horizontal translation, and the mirror holder was supported by three vertical adjustments to meet the vertical, roll and yaw adjustments. Since the pitch angle is

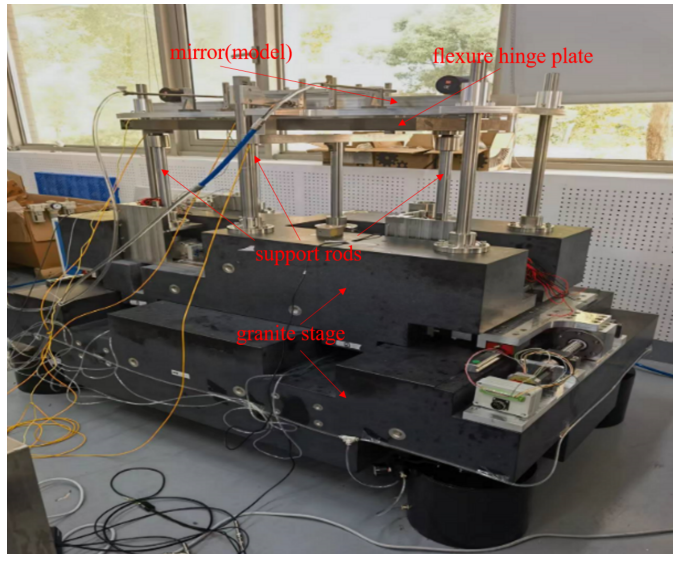

Figure 5
The prototype of the offset mirror adjustment system for the SHINE beamline.

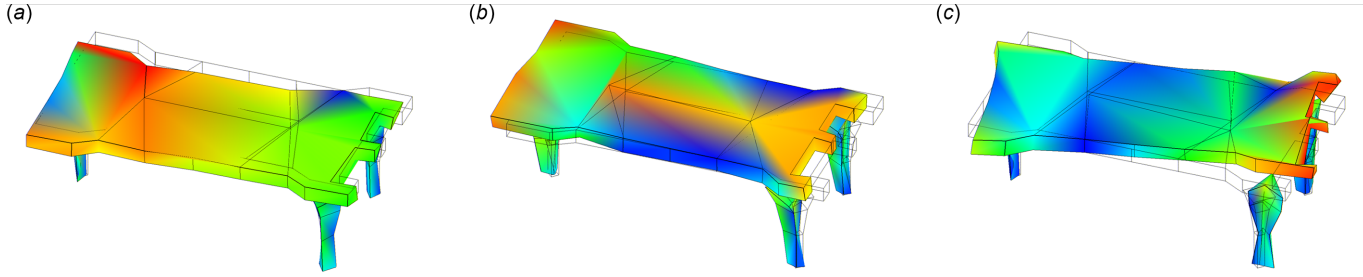

Figure 6
Modal shape at (*a*) 12 Hz, (*b*)18 Hz and (*c*) 25 Hz of the mirror regulating system.

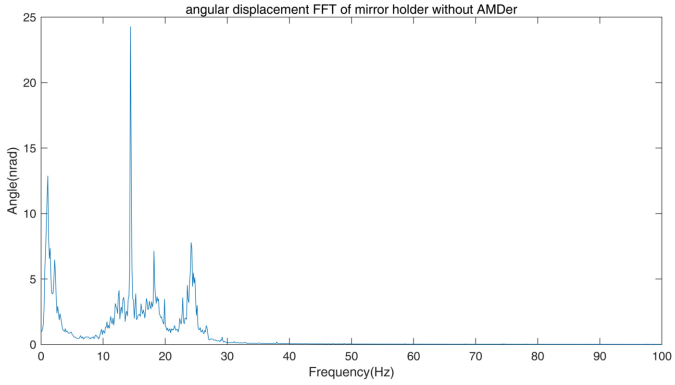

Figure 7
Vibration spectra of the offset mirror without the AMDer.

the most critical angle that we need to deflect or focus the beam, a fine pitch adjustment was designed by flexures on the mirror holder driven by a piezo actuator.

The modal of the system was measured with accelerometers (model 393B04, PCB), hammer (type INV9311) and *DASP* (version 11) software (http://www.coinv.com/product/59). The related pitch angular modes are shown in Fig. 6. The first pitch angular mode at 12 Hz and the third pitch angular mode at 24 Hz are due to stiffness differences on the ends of the mirror holder, the second angular mode at 18 Hz is attributed to the coupling of the translation, while the fourth mode at 160 Hz is from the fine pitch adjustment of the mirror holder. The absolute pitch angle vibration was calculated from the angular velocity by placing two velocity gauges (model 941B, produced by the Institute of Engineering Mechanics of China Earthquake Bureau) at a distance of 800 mm apart. The pitch angular spectrum is shown in Fig. 7, while the ground vibration in the vertical direction is shown in Fig. 8. The angular vibration below 5 Hz was attributed to ground excitations. The 14 Hz and 17 Hz vibrations were found to be external machine excitations from the ground, as they could be detected across the whole laboratory, and the spectra are rather narrow. The vibrations around 12 Hz, 18 Hz and 25 Hz are attributed to the structural modal vibrations of the adjustments. The fourth mode from the fine pitch adjustment was seen to be of little affect because of its high Eigen frequency.

3.2. Introduction of the AMDer

A 3D model of the AMDer is shown in Fig. 9; the actuator is a voice coil from Akribis (type AVM-60.25). The magnetic part is fixed to the mass, while the coil part is fixed to the base. The mass is connected to metal pieces serving as springs, and a velocity gauge (model 941B mentioned above) is also fixed to the mass for the IAVF. The signal acquisition and feedback controller is implemented in the NI cRIO-9042 RT/FPGA system: the PID controller was implemented at a 25.6 kHz sample rate. The key parameters of the AVM-60.25-type VCM and 941B-type velocity gauge are listed in Table 2. Two velocity gauges (model 941B) are fixed to the mirror holder to measure the angular velocity as

$$\dot{X}_1 = \frac{\dot{X}_{11} - \dot{X}_{12}}{L}, \tag{19}$$

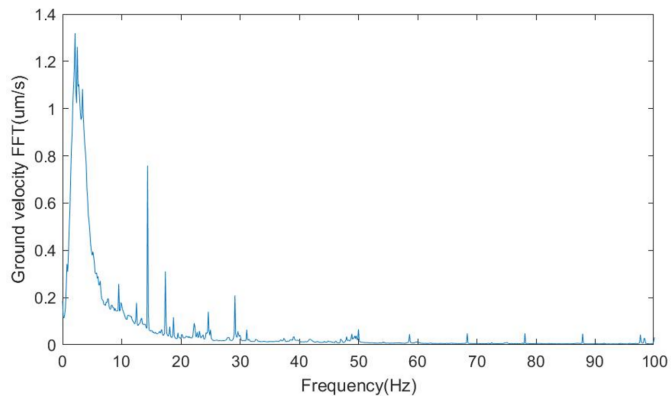

Figure 8
Ground vibration spectra in the vertical direction.

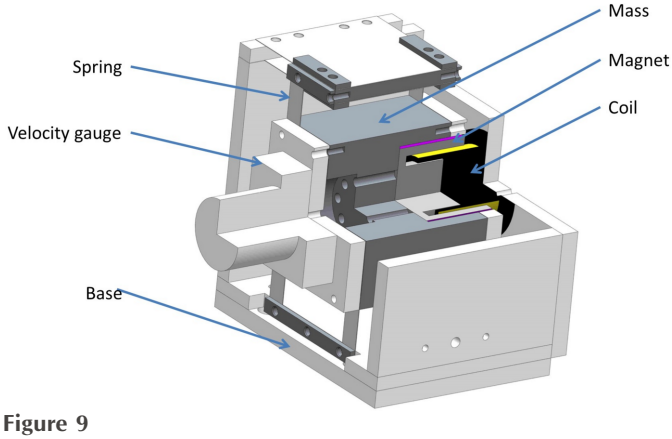

Figure 9
Structure of the AMDer.

Table 2
Parameters of the actuator, sensor and electronics.

AVM60.25 VCM force constant, K_f	17 N A^{-1}
AVM60.25 VCM resistance, R	5.35 Ω
AVM60.25 VCM inductance, L	3.82 mH
−3 db bandwidth of the 914b-type velocity gauge	1–100 Hz
Input noise of the NI 9215 module	1.2 LSB (RMS), 7 LSB (p-p)
Noise of the AD 620 In-Amp	9 nV Hz$^{-1/2}$ @ 1 kHz, 0.28 μV p-p (0.1–10 Hz)

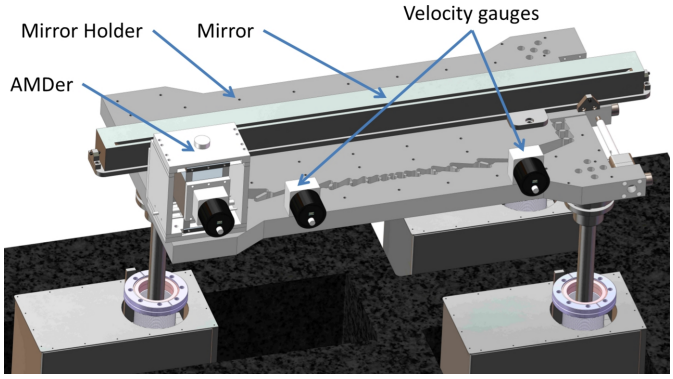

Figure 10
Test setup of the pitch angular vibration damping.

where $\dot{X}_{11}$ and $\dot{X}_{12}$ are the velocities measured by the two gauges, and L = 413 mm is the distance between the two gauges. The whole test setup is shown in Fig. 10. For easy mounting, the velocity gauges are fixed on the mirror holder rather than on the mirror dummy, because the pitch angular vibration on the mirror and the holder are almost the same by our measurement.

4. Test results and discussions

4.1. Characteristic rest

Before the performance test, the frequency response characteristics G_{OLFR} were obtained by driving the actuator with a sinusoidal frequency scanning voltage and recording the amplitude ratio

$$|\dot{X}_1(\omega)| \,/\, |U'(\omega)|$$

and phase difference

$$\varphi_{\dot{X}_1}(\omega) - \varphi_{U'}(\omega) \tag{20}$$

at each excitation frequency ω. As shown in Fig. 11, these resonant peaks agree well with the three modals contributing to the main vibration shown in Fig. 7; the peak at 6 Hz is caused by the AMDer.

In the absence of extra damping, the resonance of the AMD is only damped by the properties of the material; since the springs are made of stainless steel, the damping ratio was very small, so the open-loop response amplitude $G_s(j\omega_a)$ is too high to implement a high-gain velocity feedback, which will limit the performance of modal vibration attenuation. With IAVF

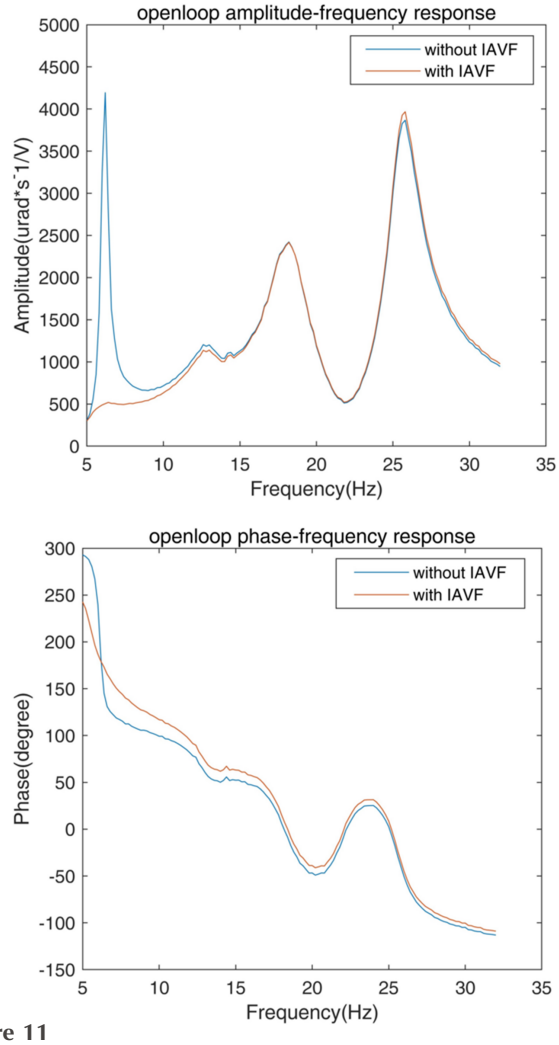

Figure 11
A comparison of the secondary path frequency response with and without IAVF.

($p_2 = -4.58 \times 10^{-5}$ μm s^{-1} V^{-1}), $G_s(j\omega_a)$ decreases significantly while the change of amplitude at the natural frequency of all the controlled structure resonance $G_s(j\omega_k)$ is negligible, which indicates that the modal vibration attenuation performance is improved.

The damping ratio was also fitted according to the waveform by the impulse response of the AMDer as shown in Fig. 12. By fitting the wave with the following equation,

$$y(t) = A \exp\left[-\xi\omega(t-t_0)\right] \sin\left[\left(1-\xi^2\right)^{1/2}\omega(t-t_0)+\varphi\right] + A_0, \tag{21}$$

the damping rate, ξ, of the resonance of the AMDer increases from 0.03 to 0.19 with IAVF.

4.2. Performance test and discussions

The pitch angular vibrations of the mirror holder measured by the two velocity gauges for different conditions are shown in Fig. 13. Spectra and the accumulated RMS are shown in the top and bottom panels, respectively, of Fig. 14. When the

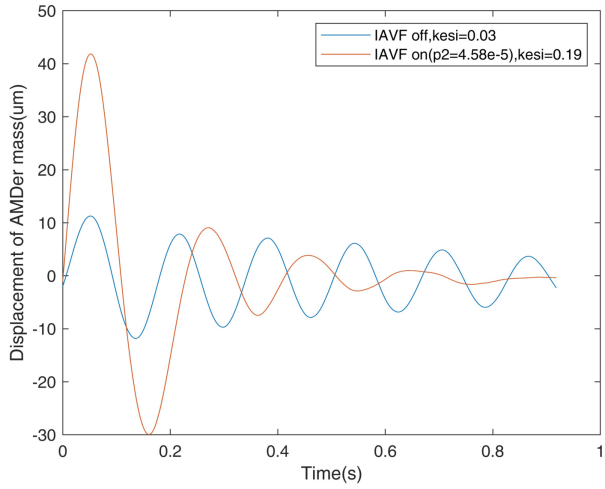

Figure 12
Comparison of the damping ratio with and without IAVF.

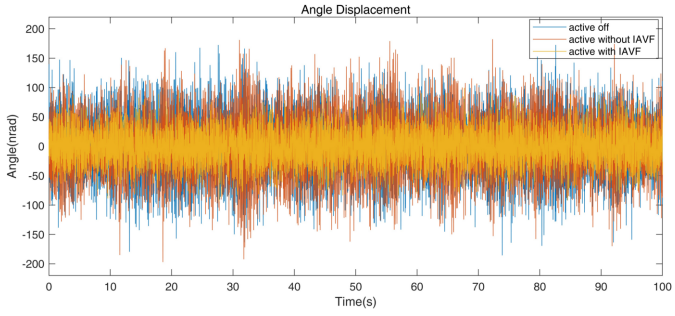

Figure 13
Angular vibration waveform comparison for the cases of active off, active without IAVF ($p_1 = 1.2 \times 10^{-4}$ µrad s^{-1} V^{-1}, $p_2 = 0$ µm s^{-1} V^{-1}) and active with IAVF ($p_1 = 9.3 \times 10^{-4}$ µrad s^{-1} V^{-1}, $p_2 = -4.58 \times 10^{-5}$ µm s^{-1} V^{-1}).

AMDer with IAVF is off, there is an additional peak at about 6 Hz compared with the spectrum in Fig. 7 without the AMDer, which is due to the natural frequency of the AMDer. Owing to the spillover effect, the damping factor with normal AMD is limited due to vibration increase at 6 Hz; the performance is then also limited. However, when the AMDer with IAVF is active, the peaks at around 6 Hz, 12 Hz, 18 Hz and 25 Hz are significantly decreased. Even at 14 Hz, the vibration caused by some external excitation is also attenuated from 26 nrad to 15 nrad. As a result, the RMS above 1 Hz of angular vibration of the mirror holder drops from 47 nrad to 27 nrad.

5. Conclusion

Active mass damping with IAVF was introduced to attenuate the structural angular vibration of a mirror system for FEL beamlines. Performance tests demonstrated that the IAVF can reduce the spillover effect and further improve the structural vibration attenuation performance. By comparing the angular vibrations with and without the active mass damping, the

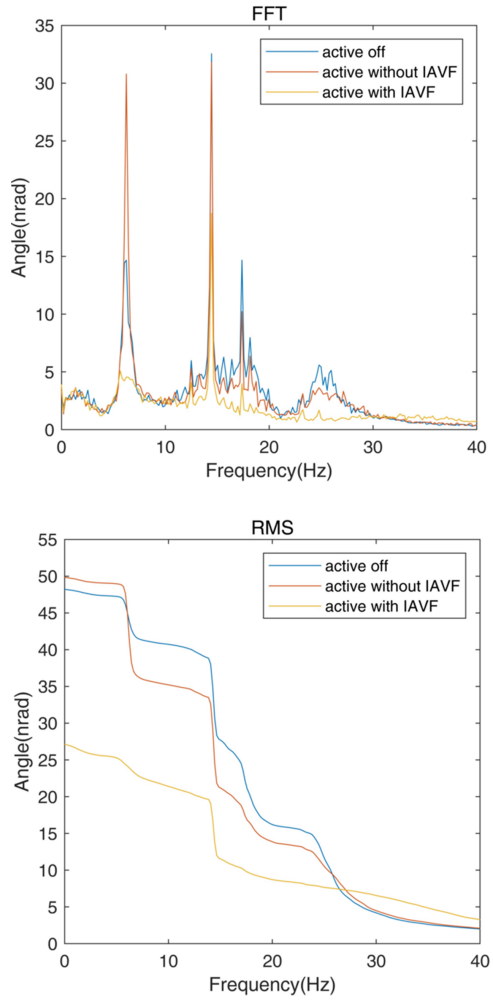

Figure 14
FFT (top) spectra and RMS (bottom) of the angular vibration comparison for the cases of active off, active without IAVF ($p_1 = 1.2 \times 10^{-4}$ µrad s^{-1} V^{-1}, $p_2 = 0$ µm s^{-1} V^{-1}) and active with IAVF ($p_1 = 9.3 \times 10^{-4}$ µrad s^{-1} V^{-1}, $p_2 = -4.58 \times 10^{-5}$ µm s^{-1} V^{-1}).

angular vibration of the mirror system was improved from 47 nrad to 27 nrad above 1 Hz in RMS.

Funding information

The research was support by the Shanghai Science and Technology Commission (Contract No. 19142202800), and the Center for Transformative Science at ShanghaiTech University.

References

Georgescu, I. (2020). *Nat. Rev. Phys.* **2**, 345.
Gonzalez Diaz, C. (2007). *Active structural acoustic control smart panel with small scale proof mass actuators*, PhD thesis. University of Southampton, UK.
Guoping, L., Yanding, W. & ZiChen, C. (2004). *Acta Armamentarii*, **25**, 462–466.
Houghton, C., Bloomer, C. & Alianelli, L. (2021). *J. Synchrotron Rad.* **28**, 1357–1363.

Li, J. W., Matias, E., Chen, N., Kim, C.-Y., Wang, J., Gorin, J., He, F., Thorpe, P., Lu, Y., Chen, W. F., Grochulski, P., Chen, X. B. & Zhang, W. J. (2011). *J. Synchrotron Rad.* **18**, 109–116.
Liu, F., Wu, T., He, S., Yuan, H., Zhang, X., Wang, Z., Li, W., Zhang, L., Chen, J., Zhu, W. (2023). *Proceedings of the 12th International Conference on Mechanical Engineering Design of Synchrotron Radiation Equipment and Instrumentation (MEDSI2023)*, 6–10 November 2023, Beijing, China. THOBM04.
Liu, R., Yu, J., Wang, G., Kang, L., Chen, J., Zhang, J., Liu, L. & Huang, L. (2020). *At. Energy Sci. Technol.* **54**, 1940–1946.
Mangra, D., Sharma, S. & Jendrzejczyk, J. (1996). *Rev. Sci. Instrum.* **67**, 3374.
Pellegrini, C. & Stöhr, J. (2003). *Nucl. Instrum. Methods Phys. Res. A*, **500**, 33–40.
Siewert, F., Buchheim, J., Gwalt, G., Bean, R. & Mancuso, A. P. (2019). *Rev. Sci. Instrum.* **90**, 021713.
Van Vaerenbergh, P., Lesourd, M., Zhang, L., Barrett, R., Eybert, L. & Mairs, T. (2008). *Design and Vibration Measurements of High Stiffness Massive Supports for the ESRF Nano-precision Engineering Platform Integration Laboratory*, https://www.researchgate.net/publication/242537400_Design_and_Vibration_Measurements_of_High_Stiffness_Massive_Supports_for_the_ESRF_Nano-precision_Engineering_Platform_Integration_Laboratory.
Zhao, Z.-T. & Feng, C. (2018). *Physics*, **47**, 481–490.